Physics of Fluids ARTICLE scitation.org/journal/phf

Evaporation from arbitrary nanoporous membrane configurations: An effective evaporation coefficient approach

Cite as: Phys. Fluids **33**, 032022 (2021); doi: 10.1063/5.0046174
Submitted: 1 February 2021 · Accepted: 3 March 2021 ·
Published Online: 25 March 2021

View Online Export Citation CrossMark

Benzi John,[1,a)] Livio Gibelli,[2] Ryan Enright,[3] James E. Sprittles,[4] Duncan A. Lockerby,[5] and David R. Emerson[1]

AFFILIATIONS

[1]Scientific Computing Department, STFC Daresbury Laboratory, Warrington WA4 4AD, United Kingdom
[2]School of Engineering, University of Edinburgh, EH9 3FB, United Kingdom
[3]Efficient Energy Transfer Department (ηET), Nokia Bell Labs, Dublin D15 Y6NT, Ireland
[4]Mathematics Institute, University of Warwick, CV4 7AL, United Kingdom
[5]School of Engineering, University of Warwick, CV4 7AL, United Kingdom

[a)]Author to whom correspondence should be addressed: benzi.john@stfc.ac.uk

ABSTRACT

Thin-film evaporation from nanoporous membranes is a promising cooling technology employed for the thermal management of modern electronic devices. We propose an effective one-dimensional analytical approach that can accurately predict the temperature and density jump relations, and evaporation rates, for arbitrary nanoporous membrane configurations. This is accomplished through the specification of an effective evaporation coefficient that encompasses the influence of different system parameters, such as porosity, meniscus shape, evaporation coefficient, and receding height. Our proposed approach can accurately predict all the typical output evaporation parameters of interest like mass flux, and temperature and density jumps, without the need to carry out computationally demanding numerical simulations. Several exemplar cases comprising of nanoporous configurations with a wide range of parameters have been considered to demonstrate the feasibility and accuracy of this analytic approach. This work thus enables a quick, efficient, and accurate means of aiding the design and engineering analysis of nanoporous membrane-based cooling devices.

I. INTRODUCTION

Evaporation at typical engineering scales is a well-researched topic with relevance to numerous industrial applications. Examples include fuel combustion in engines,[1,2] distillation processes in high-vacuum conditions,[3] and vapor-deposition processes for material coating.[4] Applications for evaporation at the nanoscale have been more recent with progress advancing with developments in micro- and nano-scale engineering and manufacturing processes. A fundamental understanding of heat and mass transfer at the kinetic scale is very important for the design and optimization of novel nano-scale applications.[5,6] One particular example is the thermal management of modern electronic devices,[7–9] where thin-film evaporation from nanoporous membranes is employed to handle the cooling process. Conventional techniques[10–13] have been found to be inadequate for the cooling of advanced radio frequency (RF) and power electronics, which reach local heat fluxes exceeding 1000 W/cm^2. Thin-film evaporation, enabled by nanoporous membranes,[14] is a novel technology with great potential as it typically offers several advantages over traditional cooling techniques that allows it to achieve high heat-flux thermal management. First, nanoporous membrane-based cooling devices[15–19] are largely self-regulating in nature since they rely mainly on capillary pressure to drive the flow. This reduces the requirement of significant pumping power to supply the liquid to the evaporating interface. Second, optimized semiconductor-based nanoporous membranes have thicknesses of the order of micrometers (typically $\sim$1 μm) and pore diameters on the order of nanometers (typically $\sim$100 nm). While smaller nanometer-sized pore diameters ensure that they generate relatively high capillary pressures, thin nanoporous membranes

reduce the flow transport length, reducing the associated viscous losses significantly. These aspects enable nanoporous membrane-based cooling devices to achieve a large critical heat flux.

A thorough understanding of the interfacial evaporation process is essential for the design of more efficient nanoporous membrane evaporative cooling devices. The performance of a nanoporous membrane evaporator is ultimately governed by the evaporation kinetics at the liquid–vapor interface. At such scales, it is critical to consider gas kinetic aspects to capture the molecular non-equilibrium effects that occur near the interface,[20] within the so-called Knudsen layer. A traditional continuum-based approach to evaluate the vapor flow within the nanopore is inadequate, as the pore size is comparable to the vapor mean free path.

From an engineering point of view, output parameters of particular interest are the evaporation rates and the temperature and density jump across the Knudsen layer, for any arbitrary set of nanoporous membrane configuration and operating conditions. The authors, in their recent work,[21] performed a comprehensive study of the nanoporous evaporation problem by carrying out extensive direct simulation Monte Carlo (DSMC) simulations. This approach captures the gas kinetic aspects by approximating solutions to the Boltzmann equation to investigate the evaporation rates and jump relations for a wide range of membrane configurations and operating conditions. Although DSMC simulations can generate high-fidelity results, it is also generally computationally intensive in nature. Additionally, the parameter space for the input variables is extremely large for the nanoporous evaporation problem, as it involves a range of variables including different meniscus shapes and positions, evaporation coefficients, porosities, interface Knudsen numbers, and far-field Mach number conditions. However, it would be of immense design benefit if all the evaporation output parameters could be predicted from simple *analytical* relations for any desired nanoporous membrane configurations and operating conditions.

To study thin-film-based nanoporous membrane cooling, there have been several reported studies analyzing evaporation in nanopores.[14,18,22–27] In particular, Lu *et al.*[24] recently demonstrated both experimentally and numerically that evaporation rates can be conveniently expressed as a function of the pressure ratio across the Knudsen layer, specifically for nanoporous configurations with relatively very low evaporation rates. However, this study was limited to low Mach number cases and did not explore the parametric effect of meniscus shape, Knudsen number, or porosity on the evaporation output parameters for different operating conditions. A state-of-the-art review of these previous works and also an extensive DSMC study of different nanoporous membrane configurations corresponding to different operating conditions are detailed in our recent work (see Ref. 21 and references therein). A notable observation from these DSMC simulations[21] is that the two-dimensionality of the flow is limited to the region next to the membrane structure, where the flow expansion phenomenon takes place. Far enough from the porous membrane, the flow is essentially one-dimensional similar to that for evaporation from an effective liquid surface. This observation has motivated the current work on investigation of an *effective* evaporation coefficient approach to predict the output parameters of interest, exploiting known analytical relations for evaporation from a planar surface.

For the case of evaporation from a *planar* surface, analytical relations exist that can predict the evaporation output parameters of interest. Planar surface cases are essentially one-dimensional and the most notable early works for this evaporation problem are from Hertz and Knudsen, and Schrage, who formulated, respectively, the classical Hertz–Knudsen formula[28,29] and Schrage relations[30] for predicting the evaporation rates. However, it is widely accepted now that both relations, although sufficient for a certain limited set of conditions, are simplistic, derived based on inaccurate assumptions and fail to relate the external macroscopic flow (vapor) variables to the physical parameters at the interface accurately.[20,31] Later works by other researchers, in particular, Labuntsov and Kryukov[32] and Ytrehus,[20] overcame these limitations by formulating gas-kinetic moment equations for the evaporation problem and derived analytical expressions for the evaporation rates and jump conditions. They related the external flow variables and interface parameters (across the Knudsen layer, typically of the order of a few mean free paths thick) through numerical solutions of moments of the Boltzmann equation. In general, the results from kinetic theoretical studies of the half-space problem of evaporation for planar surfaces using various approaches are considered to be fairly complete (e.g., see Sone[33] and references therein).

Although Labuntsov and Kryukov's and Ytrehus' analytical approach has been shown to provide good agreement with numerical solutions of the Boltzmann transport equation,[31,34] it is to be noted that this approach considers evaporation from a *planar* surface, where the flow is one-dimensional. For the one-dimensional planar case, the Knudsen number cannot be defined due to the lack of a meaningful macroscopic characteristic length. The nanoporous evaporation problem, on the other hand, is multi-dimensional in nature and dependent on the Knudsen number. As a consequence, the classic analytical equations cannot be directly employed for this problem. The multi-dimensionality of the problem is particularly obvious for significantly curved menisci and small porosity cases (where most of the surface is composed of solid, not meniscus). Likewise, receding meniscus cases, in which the meniscus moves down the pore under severe operating conditions, add further complexity due to the need to accurately describe the vapor flow within the pore.

In the present study, we propose an effective one-dimensional analytical approach that can accurately predict the temperature and density jump relations, and evaporation rates for a wide range of typical nanoporous membrane configurations. In particular, we propose an effective evaporation coefficient approach that is capable of encompassing the influence of different system parameters such as meniscus shape, evaporation coefficient, porosity, and receding height into a single effective evaporation coefficient parameter, thereby enabling the use of existing one-dimensional analytical equations for a two-dimensional nanoporous evaporation problem. Comprehensive DSMC simulations considering nanoporous configurations with a wide range of far-field conditions, porosity, Knudsen number, meniscus shape, receding heights, and evaporation coefficients have been carried out to validate and demonstrate the accuracy of the effective evaporation coefficient approach. The paper is organized as follows. Section II deals with the problem formulation and rationale for the effective evaporation coefficient approach. Section III presents computed results based on the effective one-dimensional approach and its comparison with DSMC results for a range of interface shapes and operating conditions. Finally, Sec. IV will draw conclusions from the present study.

II. PROBLEM FORMULATION

In this section, the nanoporous membrane configurations considered, the computational setup for the DSMC simulations, and the rationale for the effective evaporation coefficient approach are detailed. A wide range of meniscus shapes and operating conditions have been considered to demonstrate the feasibility of the effective one-dimensional analytical approach using an effective evaporation coefficient. DSMC simulations have been carried out to demonstrate the accuracy of the effective approach and for validation purposes.

A. Mathematical and computational setup

A schematic of the nanoporous membrane configuration is shown in Fig. 1. A unit nanoporous membrane configuration, periodic in the x-direction, that is representative of the entire system of pores is considered. The nanopore porosity is defined as $\phi = L_p/(2W + L_p)$, where L_p is the width of the pore and W represents the width of the pore walls on either side of the meniscus. A porosity of unity represents the limiting case with no walls, i.e., $W = 0$. Variation in ϕ is achieved by fixing L_p, the characteristic length scale in our problem, and changing W. As illustrated in Fig. 1, five meniscus shapes are considered. The meniscus represents the liquid–vapor interface where evaporation takes place. The curved meniscus cases have a larger interfacial surface compared to the flat meniscus case, which is expected to alter the evaporation dynamics. The interface surface length (S), contact angle (θ), and radius of curvature (R) for a representative meniscus are illustrated in Fig. 2, where S is defined by $S = L_p \frac{\theta}{\sin(\theta)}$. The contact angles, $\theta = 0^\circ$ and $\theta = 90^\circ$ represent the extreme scenarios of flat (S_1) and semicircle (S_5) interfaces, respectively. The intermediate cases of curved interfaces in Fig. 1 of S_2, S_3, and S_4 have a contact angle of 30°, 60°, and 75°, respectively.

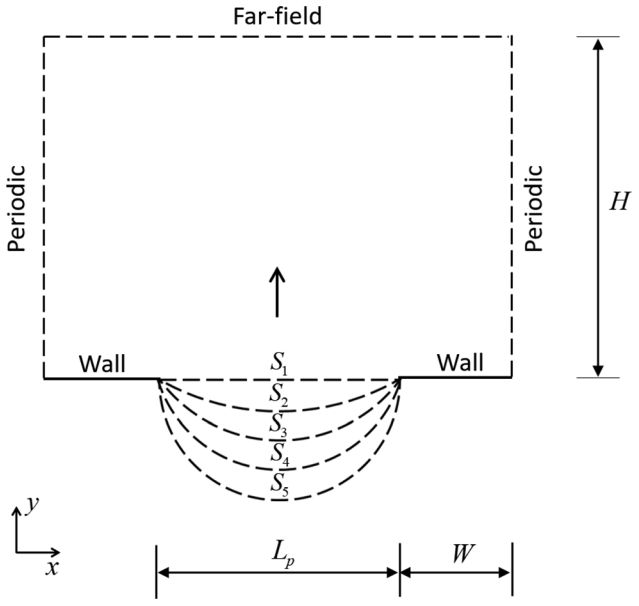

FIG. 1. Schematic of the computational geometry (not to scale).

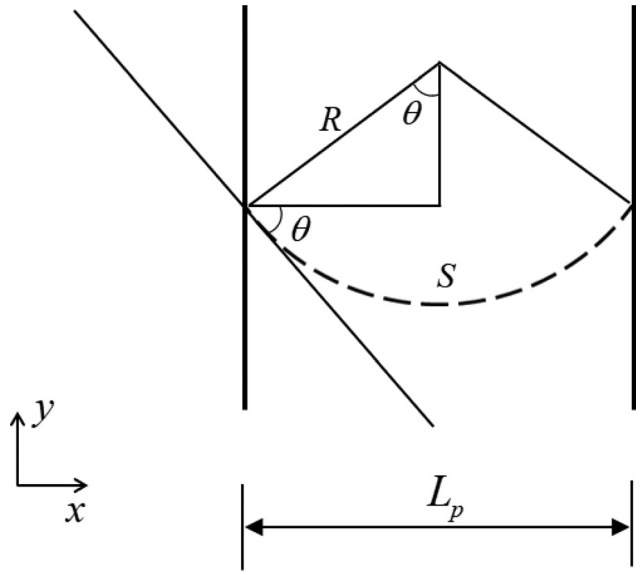

FIG. 2. Schematic of a representative meniscus showing the interface surface length (S) and contact angle (θ).

At the interface, a constant saturation pressure, P_s, and temperature, T_s, are imposed. The Knudsen number is based on the interface operating conditions and defined as $Kn = \lambda/L_p$, where λ is the mean free path. The variation in Kn is achieved by fixing L_p and changing the operating pressure at the interface.

At the interface (meniscus) boundary, a half-range Maxwellian is employed to specify the distribution function of evaporating (i.e., "outward") molecules[35]

$$f_e(\boldsymbol{c}) = \sigma \frac{n_s}{(2\pi \mathrm{R} T_s)^{3/2}} \exp\left(-\frac{\boldsymbol{c}^2}{2\mathrm{R}T_s}\right), \quad \boldsymbol{c}\cdot\boldsymbol{n} > 0. \tag{1}$$

Here n_s is the saturated vapor number density, R is the specific gas constant, and σ is the evaporation coefficient. The normal unit vector of the interface, pointing into the vapor, is denoted by $\boldsymbol{n}$. Maxwell's gas-surface scattering kernel, $J(\boldsymbol{c}', \boldsymbol{c})$, is used to describe the molecular re-emission at the interface, i.e., vapor molecules with incoming velocity $\boldsymbol{c}$ are instantaneously changed to $\boldsymbol{c}'$ upon interacting with the condensed phase at the interface

$$J(\boldsymbol{c}',\ \boldsymbol{c}) = (1-\sigma)\left[\alpha(\boldsymbol{c}'\cdot\boldsymbol{n})\frac{1}{2\pi(\mathcal{R}T_s)^2}\exp\left(-\frac{\boldsymbol{c}'^2}{2\mathcal{R}T_s}\right) + (1-\alpha)\delta\left(\boldsymbol{c}'-\boldsymbol{c}+2(\boldsymbol{c}\cdot\boldsymbol{n})\boldsymbol{n}\right)\right]. \tag{2}$$

The evaporation coefficient, σ, specifies the fraction of vapor molecules interacting with the interface and absorbed. Hence, $(1-\sigma)$ represents the total fraction of impinging molecules that are instantaneously re-emitted, α being the probability of diffuse re-emission, and $(1-\alpha)$ the probability of specular reflection. For all cases considered in this work, fully diffuse molecular re-emissions are considered at the interface (i.e., $\alpha = 1$).

The boundary conditions at the far-field boundary need to be considered carefully, as for the evaporation problem, only one parameter can be freely specified; the other parameters need to be extracted as outcomes of this single driving parameter.[30] The equilibrium state attained by the vapor at the far-field[35] can be described by the drifted Maxwellian distribution, $f_\infty(\boldsymbol{c})$,

$$f_\infty(\boldsymbol{c}) = \frac{n_\infty}{(2\pi\mathcal{R}T_\infty)^{3/2}} \exp\left(-\frac{(\boldsymbol{c} - U_\infty\hat{\boldsymbol{y}})^2}{2\mathcal{R}T_\infty}\right). \tag{3}$$

Here, n_∞, T_∞, and U_∞ are the number density, temperature, and velocity, respectively, at far-field conditions and $\hat{\boldsymbol{y}}$ is the unit vector in the y-direction (i.e., normal to the boundary). For later reference, the far-field Mach number, Ma_∞ is defined as $U_\infty/\sqrt{\kappa\mathcal{R}T_\infty}$, where κ is the specific heat ratio. In this work, the far-field velocity, U_∞, has been imposed at the far-field by forcing the velocity distribution function at the far-field boundary to be symmetric with respect to U_∞.[36]

All simulations in this work have been carried out using SPARTA,[37,38] a highly scalable parallel open-source DSMC code. Argon gas was considered, for simplicity, in conjunction with the variable hard sphere (VHS) collision model. The simulations consider the evaporation of argon from the interface into its own vapor. The particle–wall interactions are considered to be fully diffuse at a constant wall temperature, T_s. To enable the nanoporous evaporation simulations, we have implemented the interface evaporation and far-field boundary conditions in SPARTA and also have followed the well-known guidelines with respect to the cell size, time step, and particle numbers that are needed for accurate DSMC calculations.[39]

The choice of saturation pressure and temperature for our simulations is explained next. The kinetic boundary condition at the liquid–vapor interface describing the distribution function of evaporating molecules is a half-range Maxwellian [Eq. (1)] with the saturated vapor density (n_s) and the liquid bulk temperature (T_s). In reality, the saturated vapor density depends on the liquid bulk temperature but, in fact, it can be noted that n_s and T_s appear as independent parameters in Eq. (1). Therefore, in practice, the choice of P_s and T_s is not very critical for the accurate prediction of non-dimensional evaporation output parameters, for a given operating condition. For all the simulations considered in this work, a constant value of T_s is used, i.e., $T_s = 273$ K, but the saturation pressure is varied as in Table I.

B. The effective evaporation coefficient approach

For the case of evaporation from a *planar* surface [or equivalently, a nanoporous configuration which has a flat meniscus (S_1) with a porosity of unity], analytical relations have been derived which permits one to accurately predict output parameters like the evaporation rates (mass flux), and the density jump and temperature jump across the Knudsen layer, for arbitrary values of evaporation coefficient. For the evaporation rates and temperature jump output parameters in this study, we appeal to the one-dimensional analytical equations for evaporation from a planar surface by Labuntsov and Kryukov.[32] The mass flux, M_{1D} and temperature jump, T_∞/T_s for evaporation from a planar surface are given by

$$M_{1D} = 0.6C_s\left(\frac{\rho_\infty}{\rho_0}\right)^{1/2}(\rho_0 - \rho_\infty), \tag{4}$$

$$\frac{T_\infty}{T_s} = 1 - 0.265\ \frac{\rho_0 - \rho_\infty}{\sqrt{\rho_0\rho_\infty}}, \tag{5}$$

where the interface density, ρ_0 for arbitrary values of evaporation coefficient, σ is expressed as

$$\rho_0 = \left(1 - 2\sqrt{\pi}\frac{M_{1D}}{\rho_s C_s}\frac{1-\sigma}{\sigma}\right)\rho_s. \tag{6}$$

Here, $C_s = \sqrt{2\mathcal{R}T_s}$, where $\mathcal{R}$ is the specific gas constant. The terms ρ_s and ρ_∞ are the saturation and far-field densities, respectively.

For the density jump, ρ_s/ρ_∞ across the Knudsen layer for a planar surface, we follow the one-dimensional analytical expression formulated by Ytrehus[20] for arbitrary values of evaporation coefficient. This can be expressed in terms of the far-field velocity, U_∞ as

$$\frac{\rho_s}{\rho_\infty} = \left(\frac{\rho_s}{\rho_\infty}\right)_{1D} + \frac{1-\sigma}{\sigma}2\sqrt{\pi}\frac{U_\infty}{\sqrt{2\mathcal{R}T_s}}, \tag{7}$$

where $(\rho_s/\rho_\infty)_{1D}$ is the density jump for an evaporation coefficient of unity, corresponding to the one-dimensional case for the same U_∞.

For the effective evaporation coefficient approach proposed in this study, we extend the use of the above analytical equations for evaporation from a planar surface [Eqs. (4)–(7)], to also predict the evaporative mass flux and jump relations for any arbitrary nanoporous membrane configuration. This is made possible through the specification of an appropriate effective evaporation coefficient, σ_{eff} which relates the porosity of the membrane to the actual evaporation coefficient, σ. More specifically, the evaporation coefficient, σ in these expressions is replaced by an appropriate effective evaporation coefficient, σ_{eff}, which encompasses the effects of different system parameters into a single effective parameter. The rationale for testing this approach mainly stems from the equivalence between the parameters, evaporation coefficient and porosity, and the overall one-dimensional nature of the nanoporous flow. The evaporation coefficient essentially determines the actual rate of evaporation relative to the maximum possible evaporation rate from the interface per unit area. Likewise, porosity also has a similar meaning as it describes the available interface area for evaporation over the total membrane surface area. It can be thus intuitively understood that both porosity and evaporation coefficient are very similar in their effect on the overall mass transfer process. Additionally, DSMC simulations from our previous work[21] have demonstrated that the two-dimensionality of the flow is limited to the region next to the membrane structure, where the flow expansion phenomenon takes place. Sufficiently far away from the porous membrane, the flow is essentially one-dimensional, similar to that for evaporation from an effective liquid surface for ϕ=1.

This observation opens up the possibility of a one-dimensional effective evaporation approach, by relating the porosity of the

TABLE I. Saturation pressure, P_s, considered for different Knudsen numbers.

Kn	P_s (Pa)
0.05	52 500
0.1	26 250
1	2625
10	262.5

membrane to the actual evaporation coefficient. The choice of σ_{eff} depends on the nanoporous membrane configuration under consideration. For the flat meniscus case and arbitrary values of evaporation coefficient and porosity, the proposed effective evaporative coefficient to be specified is $\sigma_{eff} = \sigma \times \phi$. For curved and receding interfaces, the influence of different parameters like meniscus shape, evaporation coefficient, porosity, and receding heights is again encompassed by a single effective evaporation coefficient parameter, but with the aid of more complex, yet comprehensive, empirical expressions. The feasibility and accuracy of this approach for different operating conditions and choice of the effective evaporation coefficient for different nanoporous membrane configurations will be further detailed in Sec. III.

III. RESULTS AND DISCUSSION

The feasibility and accuracy of the effective evaporation coefficient approach will be discussed in this section by considering a range of nanoporous configurations and parameters. DSMC results will be employed for comparison and validation purposes. The flat meniscus case will be considered in detail first (Sec. III A), for a wide range of far-field Mach numbers, interface Knudsen numbers, and evaporation coefficients. In Sec. III B, a detailed analysis will be carried out for the relatively small Knudsen number cases to explain why the effective evaporation approach loses accuracy in this flow regime. The effective approach for the curved interfaces for selected operating conditions is detailed in Sec. III C. Finally, Sec. III D will deal with the effective one-dimensional approach for the receding meniscus cases. Unlike the flat interface case, only selected high Knudsen number cases will be considered for the receding and arbitrary meniscus shapes, since transition and free-molecular regimes are the main regimes of interest for the nanoporous membrane application considered in the present work, and also for the sake of brevity.

A. The flat meniscus

The evaporation rate and jump relations for the *flat* meniscus, S_1, are investigated first for an evaporation coefficient of unity ($\sigma = 1$). The effective evaporation coefficient σ_{eff} considered for the flat interface with a unity evaporation coefficient is simply set as $\sigma_{eff} = \phi$, regardless of the far-field velocity considered. Figure 3 shows the variation in computed mass flux as a function of Mach number, predicted by both the effective sigma approach and DSMC, for three selected Knudsen numbers (i.e., $Kn = 0.05$, 1, and 10). Three different porosities are considered, i.e., $\phi = 0.75$, 0.5, and 0.25. The mass flux values here have been normalized against the ideal case of evaporative mass flux from a planar surface for an evaporation coefficient of unity, M_{1D}, given in Eq. (4). It can be noted that reductions in the value of porosity can lead to substantial reductions in mass flux, particularly as Ma_∞ increases. This can be attributed to the combined effect of a relative decrease in the available evaporative surface as porosity decreases and the increased role of gas expansion near the interface.[21]

A very good agreement for the mass flux can be noted between the effective sigma approach and the DSMC results for the higher Knudsen number cases (transition regime and beyond, i.e., $Kn = 1$ and $Kn = 10$) while discrepancies can be noted for relatively low Knudsen numbers in the slip regime ($Kn = 0.05$), for all porosities. For $Kn = 0.05$, the analytical mass flux based on σ_{eff} under predicts at low Mach numbers, while at higher Mach numbers it slightly over shoots the DSMC mass flux. The corresponding plots comparing the density and temperature jumps are shown in Figs. 4 and 5. It can be noted that for the density jump (Fig. 4), the comparison at intermediate and relatively high Knudsen numbers is again excellent, while for low Knudsen numbers (i.e., $Kn = 0.05$) some discrepancies can be noted. As for the temperature jump (Fig. 5), an overall excellent agreement is observed except for small Knudsen numbers where deviations clearly show up. The deviations noted in Fig. 5 for $Kn = 0.05$ may be attributed to the sensitivity of the analytical temperature-jump relations [Eqs. (5) and (6)] to the value of the mass flux, for which there is a discrepancy between the numerical and analytical estimates (as discussed before). From Fig. 5, it can be also noted that as Ma_∞ increases, the far-field temperature drops substantially. Interestingly, for a fixed Ma_∞, the temperature jump does not depend on the porosity. Additionally, at relatively low Mach numbers, the comparison between the effective sigma approach and the DSMC results is very good for $Kn = 1$ and $Kn = 10$. Deviations can, however, be noted for the temperature jump near the sonic flow limit ($Ma_\infty \to 1$). The discrepancy may be explained by the slight inaccuracy of the moment solution near the sonic flow limit, which is a known issue previously reported in the literature.[31] The discrepancy can be noted in previous works (e.g., Frezzotti[36]) where, for example, at $Ma_\infty = 0.956$, the predicted temperature jump from the DSMC method is given as $T_\infty/T_s = 0.656$. However, for the same far-field density conditions, the analytical relation predicts $T_\infty/T_s = 0.694$.

We now apply the effective one-dimensional analytical approach to the flat meniscus with *arbitrary* values of evaporation coefficient. Although $\sigma = 1$ is considered generally to be a reasonable assumption, previous experimental and theoretical studies[40–45] suggest that it is also possible for the evaporation coefficient to be significantly less than one under certain conditions, particularly for polyatomic gases like water, methanol, and refrigerants. The effective evaporation coefficient σ_{eff} considered for the flat interface with arbitrary values of σ is $\sigma_{eff} = \phi \times \sigma$. A fixed far-field velocity, $U_\infty = 60$ m/s, is considered for all simulations in this part of the study, as we now focus on investigating the evaporation output parameters as a function of the evaporation coefficient ($0.1 \le \sigma \le 1$). Three values of porosity are again considered, i.e., $\phi = 0.75$, 0.5, and 0.25, as well as a range of evaporation coefficients and Knudsen numbers. Figures 6–8 show the variation in evaporation rates, density, and temperature jump values as a function of the evaporation coefficient for three selected Knudsen numbers, i.e., $Kn = 10$, 1, and 0.1, respectively. A very good agreement has still been found between the effective sigma approach and the DSMC results for the higher Knudsen number cases, i.e., $Kn = 1$ and $Kn = 10$, for all values of σ. However, discrepancies can be noted for the low Knudsen number case, $Kn = 0.1$, for higher values of evaporation coefficient, particularly as $\sigma \to 1$. Deviations can be noted, in particular, for the temperature-jump values, similar to that observed for the $\sigma = 1$ case. This can be again attributed to the sensitivity of the analytical temperature-jump relations [Eqs. (5) and (6)] to the value of the mass flux at low Knudsen numbers. However, as $\sigma \to 0$, the comparison between the analytical and DSMC results is very good, for all the evaporation output parameters considered.

To summarize the results of this section, the effective one-dimensional analytical approach works accurately for a flat interface for sufficiently large Knudsen numbers ($Kn > 0.1$) using an effective evaporation coefficient parameter defined as $\sigma_{eff} = \phi \times \sigma$ for all

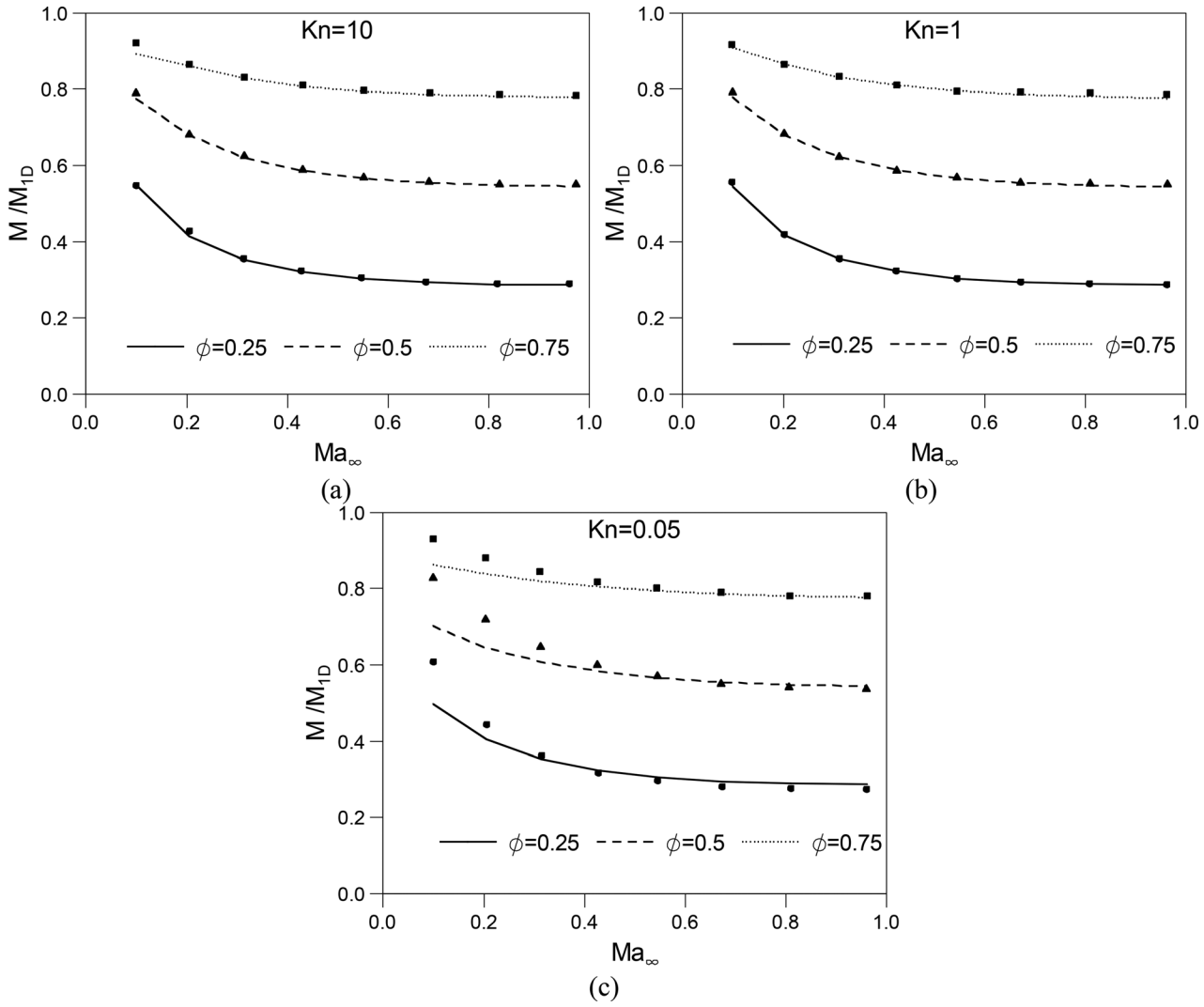

FIG. 3. Normalized mass flux vs far-field Mach number for three different Knudsen numbers: (a) Kn = 10, (b) Kn = 1, and (c) Kn = 0.05, when $\phi < 1$. The lines represent the analytical results; the symbols represent the DSMC results.

far-field conditions. The discrepancies noted at smaller *Kn* are addressed in Sec. III B.

B. Effective approach at low Knudsen numbers

The effective sigma approach has been found to be less accurate in low, compared to high, Knudsen number cases. Additionally, the discrepancies at low *Kn* were noted to be significantly higher for low far-field velocities when compared to those at higher velocities (see Fig. 3). A possible explanation for this can be drawn by contrasting the nature of flow dynamics near the interface for different Knudsen number conditions. Unlike in the high *Kn* regime (collision-less flow limit), low Knudsen numbers are collision dominated and are often characterized by a viscous layer in the near-interface region that supports shear stresses and momentum diffusion. This effectively implies that the one-dimensionality of flow underlying the effective evaporation approach holds much better for the high *Kn* cases when compared to the low Kn cases. The better accuracy for the very high far-field velocity cases at low *Kn* values could be intuitively attributed to the fact that with a high flow speed, gas molecules travel mostly unidirectionally very fast with comparatively less time to collide and diffuse from the main flow direction into the transverse flow direction. This aspect associated with very high far-field velocity cases also favors the overall one-dimensionality of the flow near the interface, making it more amenable to the effective one-dimensional approach when compared to the low far-field velocity cases.

We now examine the velocity flowfield and streamlines at two extreme Knudsen numbers, $Kn = 0.05$ and $Kn = 10$, to identify the overall differences in the flow expansion nature near the interface for various porosities ($\phi = 0.75$, 0.5, and 0.25). The velocity field overlaid

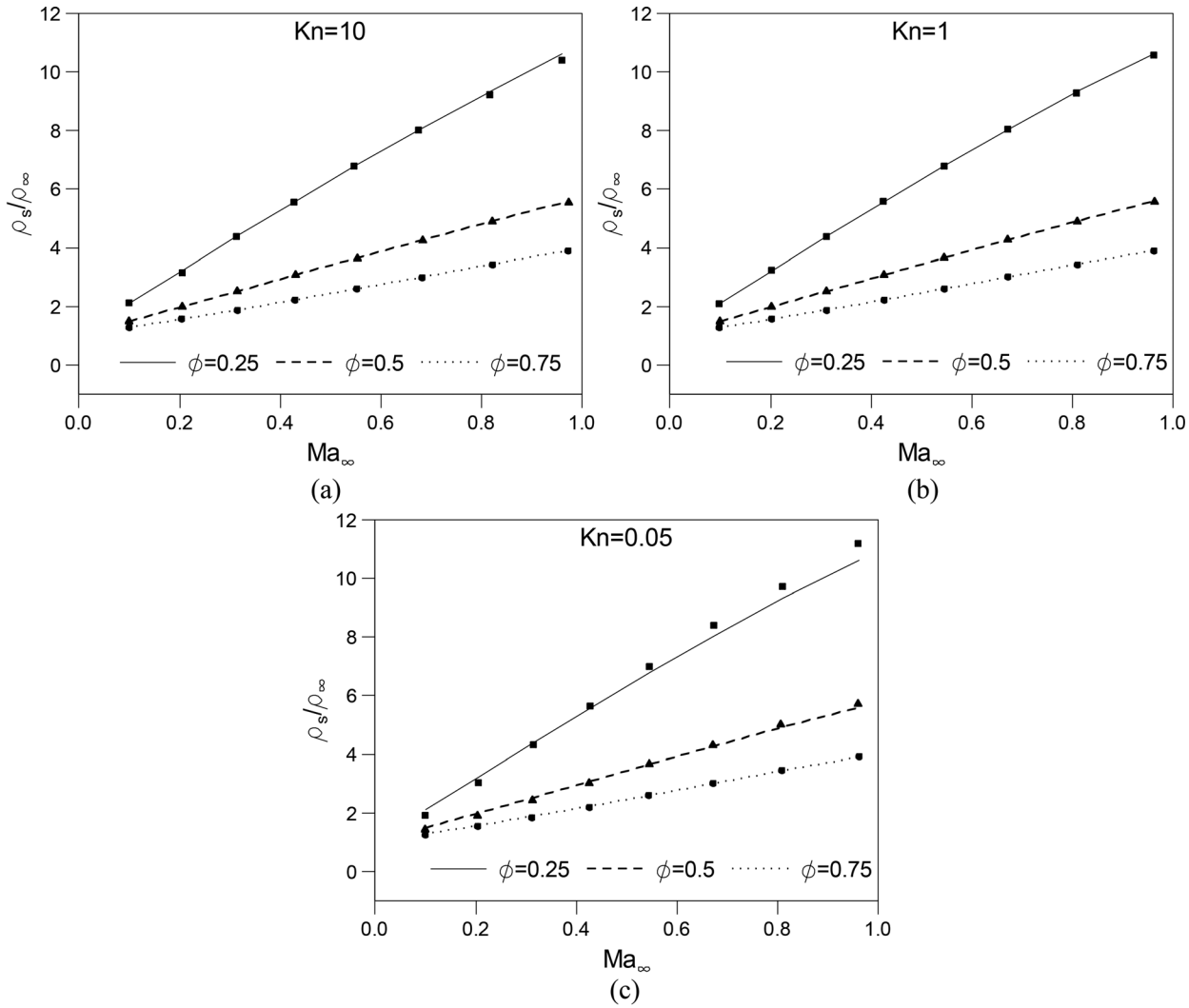

FIG. 4. Density jumps (ratios) across the Knudsen layer vs far-field Mach number for different Knudsen numbers: (a) Kn = 10, (b) Kn = 1, and (c) Kn = 0.05, and porosities. The lines represent the analytical results; the symbols represent the DSMC results.

with streamlines for the different cases considered is shown in Fig. 9. It can be noted from the streamlines, for porosities close to unity ($\phi = 0.75$), that the flow-field is mostly one-dimensional for both Knudsen numbers. However, for small values of porosity, the flow-field next to the interface becomes strikingly different at low values of *Kn*. In particular, the flow-field is mostly two-dimensional for the case, $\phi = 0.25$ and Kn = 0.05, with the existence of a pair of Moffatt eddies[46] in the corners. However, for larger Knudsen numbers ($Kn = 10$), the two-dimensionality of flow near the interface is comparatively minimal even at very low porosities [see Fig. 9(f)]. This again implies that the loss of accuracy at low degrees of flow rarefaction, particularly for low values of porosity, reflects the fact that the overall one-dimensionality of flow underlying the effective evaporation coefficient approach breaks down at low Knudsen numbers.

To understand the interfacial processes at different Knudsen numbers further, we investigate the normalized evaporative mass flux vs Knudsen number plot for different porosities at a selected constant far-field velocity, $U_\infty = 60$ m/s and $\sigma = 1$. This is shown in Fig. 10. It is clear that, unlike for a porosity of unity ($\phi = 1$), the mass flux is *not* independent of the Knudsen number for the $\phi < 1$ cases. At relatively low Knudsen numbers, the evaporation rates are noted to increase compared to the high Knudsen number cases. This implies that the effective sigma approach will not be equally valid at all Knudsen numbers when $\phi < 1$. To delve deeper, we examine the interfacial processes (in particular, the condensation rates and the vapor velocity next to the interface) that ultimately impacts the evaporation rates at different Knudsen numbers. We consider a specific case $\phi = 0.5$, $U_\infty = 60$ m/s and evaporation coefficient of unity at different Knudsen numbers ($Kn = 0.05$, 0.1, 1, and 10) for this purpose.

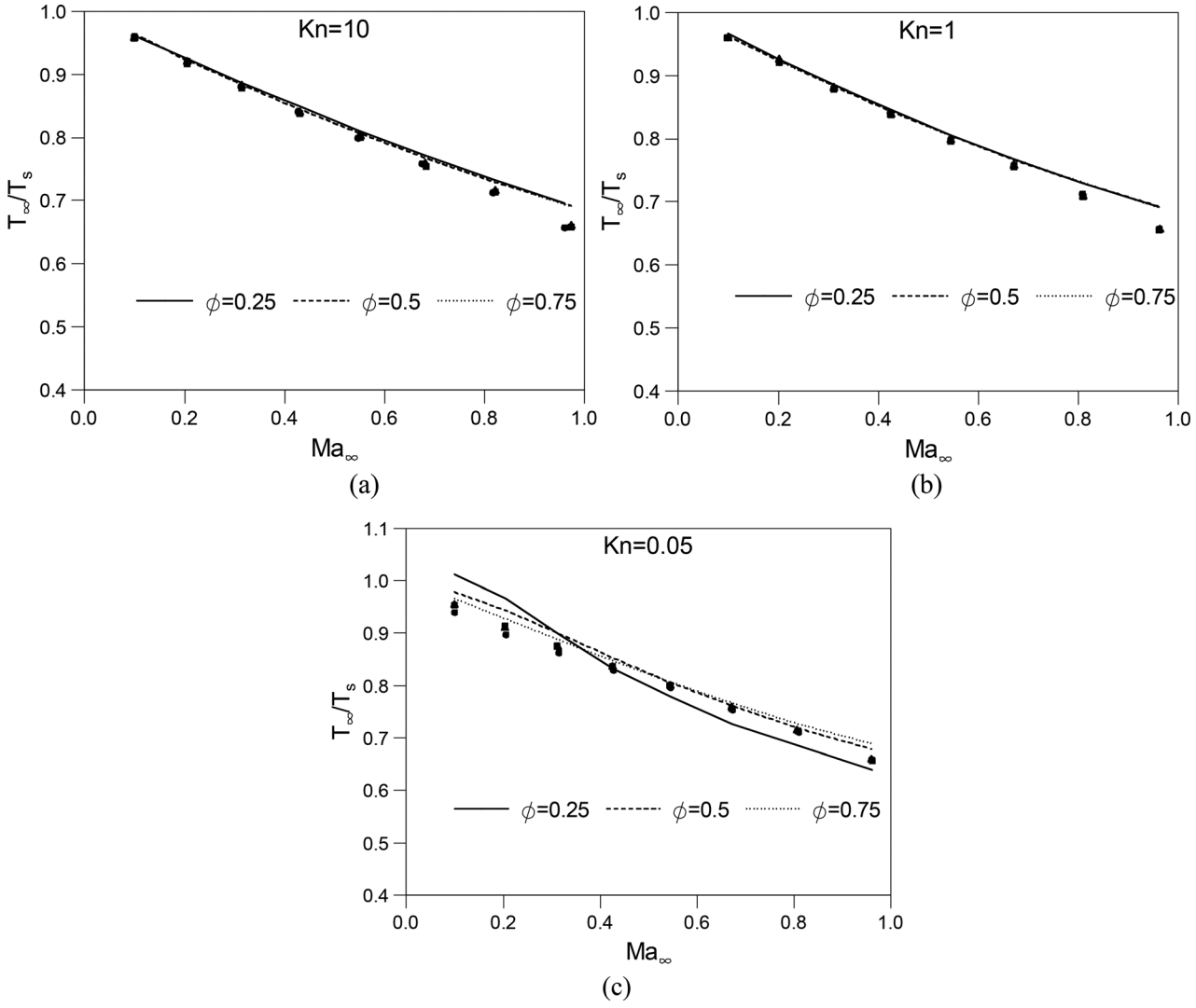

FIG. 5. Temperature jumps (ratios) across the Knudsen layer vs far-field Mach number for different Knudsen numbers: (a) Kn = 10, (b) Kn = 1, and (c) Kn = 0.05, and porosities. The lines represent the analytical results. The symbols represent the DSMC results; the square, triangular, and circular symbols represent the results for $\phi = 0.25$, 0.5, and 0.75, respectively.

Evaporation rates are ultimately dependent on the interfacial processes, and therefore here we examine the condensation flux at the interface for different Knudsen numbers. The normalized condensation rate of the vapor molecules at the interface, $M_C = M_{cond}/M_e$, has been formulated as follows. The rate at which molecules condense on the evaporating interface (condensation rate, M_{cond}) is calculated as

$$M_{cond} = \frac{mN\eta}{Adt}. \tag{8}$$

Here m is the mass of a vapor molecule, N is the number of molecules crossing the interface from the vapor side of the interface, η is the ratio of physical particles to simulation particles, A is the interface surface (i.e., area per unit width), and dt is the time step. The condensation rate has been normalized with respect to the analytical expression for total emitted evaporative mass flux from a given surface, M_e, given by

$$M_e = \sigma\rho_s\sqrt{\frac{\mathcal{R}T_s}{2\pi}}. \tag{9}$$

The computed condensation rates, M_C, for the flat meniscus at different values of Kn and $\phi = 0.5$, $U_\infty = 60$ m/s are shown in Table II. Clearly, the condensation rates at the interface are dependent on the Knudsen number. At low Knudsen numbers, the condensation rates (losses) are lower, consistent with the higher evaporative mass flux at these conditions noted in Fig. 10. The reason for this can be understood by examining the flow expansion phenomenon (in particular, the vapor velocity profile) near the interface for the different

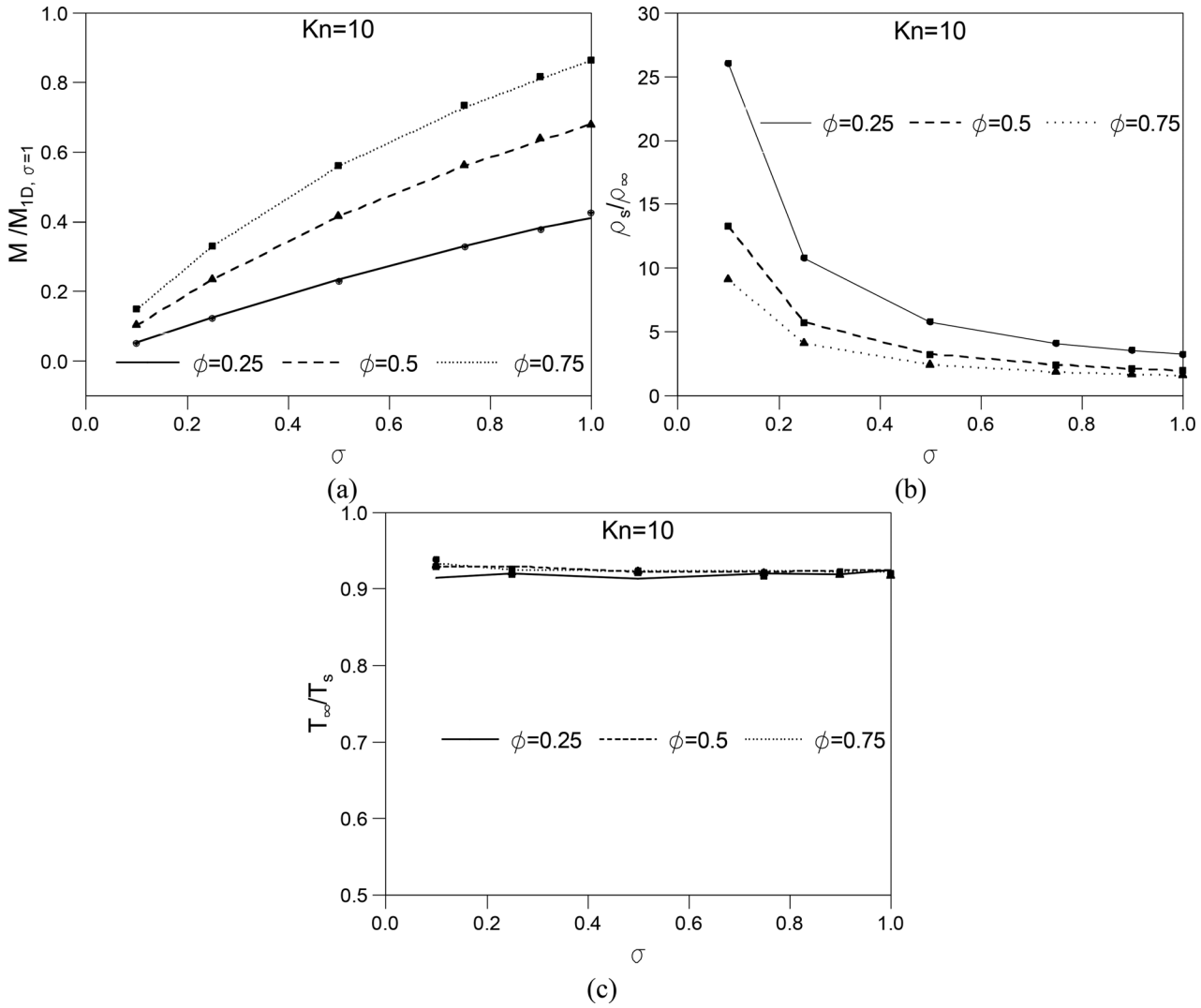

FIG. 6. (a) Normalized mass flux, (b) density jump, and (c) temperature jump vs the evaporation coefficient for $Kn = 10$ and $U_\infty = 60$ m/s when $\phi < 1$. The lines represent the analytical results; the symbols represent the DSMC results.

Knudsen numbers. The variation of the normalized velocity and density profile along the extent of the domain (in the *y*-direction) is shown in Fig. 11. The domain extent is normalized with respect to the mean free path for the respective Knudsen number under consideration. It can be noted that the flow expansion varies with *Kn*. In particular, it can be observed that on the *mean free path scale* considered, downstream equilibrium conditions (particularly the far-field velocity conditions) are attained at a much shorter distance from the interface for the larger *Kn* cases. Additionally, it is apparent that as the Knudsen number reduces, the magnitude of flow velocity near the interface is substantially higher (the higher peak velocities at low-*Kn* can be also noted from the flowfield in Fig. 9). The higher the flow velocities are near the interface, the higher the probability for molecules to travel unidirectionally (i.e., in the flow direction) and, therefore, the condensation rate at the interface reduces. The larger evaporative mass flux at lower *Kn* is consistent with the lower interfacial condensation rates for these conditions, which in turn is due to the significantly higher flow velocity (that favors a larger unidirectional flow of molecules) near the interface.

In this section, it has been found that the flow expansion characteristics at low Knudsen numbers are substantially different from that at higher Knudsen numbers for $\phi < 1$ cases. In particular, low-*Kn* flows (i.e., in the near-continuum and slip regime) are collision dominated and as a result, the flow next to the interface is predominantly two-dimensional in nature. On the other hand, for high-*Kn* flows (i.e., in the transition regime and beyond), the corresponding two-dimensional effects are relatively minimal in the near-interface region, implying that the overall one-dimensionality underlying the effective evaporation approach holds much better at these conditions when compared to low-*Kn* flow conditions. Additionally, the varying vapor

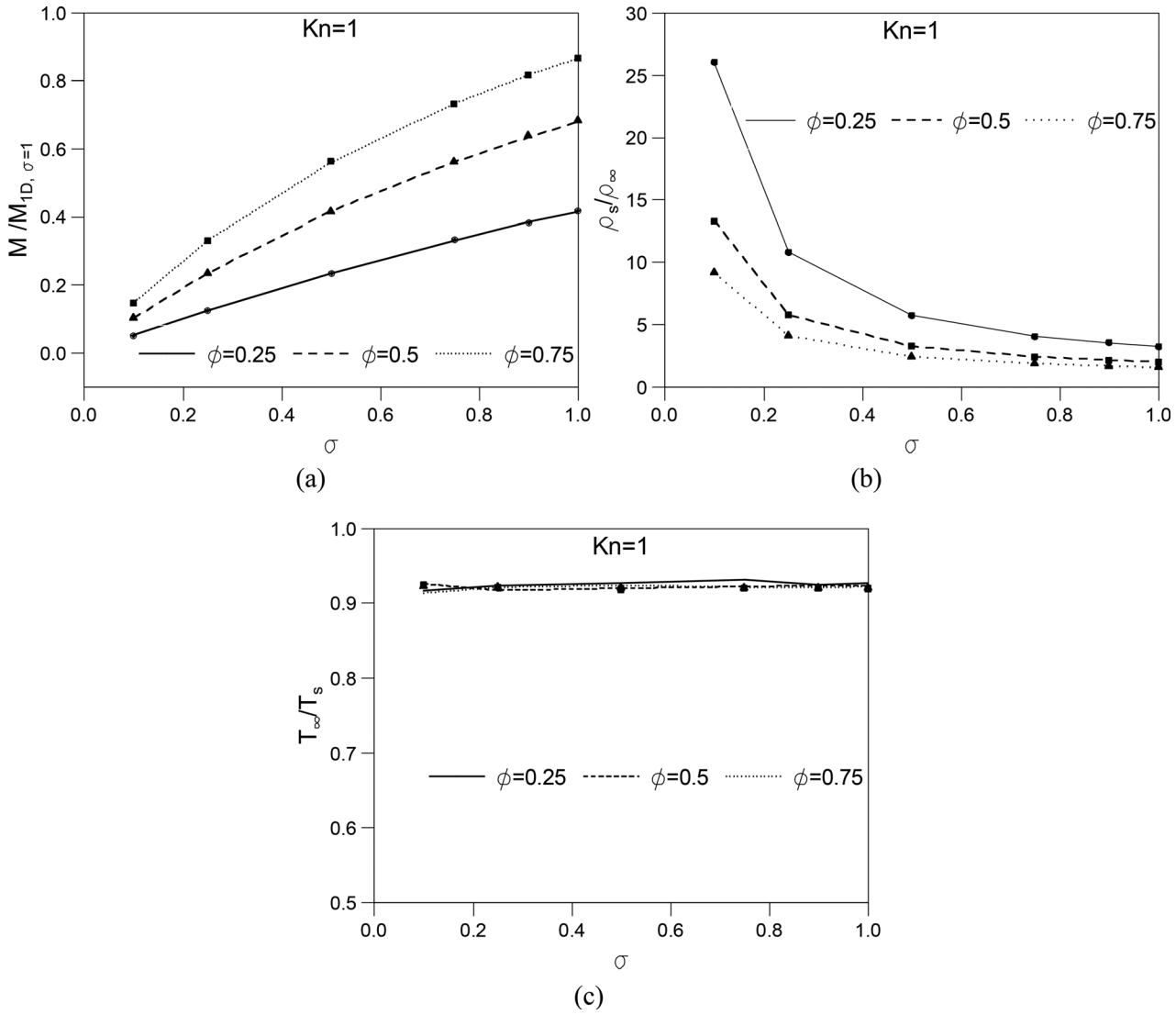

FIG. 7. (a) Normalized mass flux, (b) density jump, and (c) temperature jump vs the evaporation coefficient for $Kn = 1$ and $U_\infty = 60$ m/s when $\phi < 1$. The lines represent the analytical results; the symbols represent the DSMC results.

expansion characteristics near the interface at different Knudsen numbers result in evaporation rates that are *dependent* on the Knudsen number. This can be mainly attributed to the differences in the interfacial processes and vapor expansion characteristics with variation in *Kn*; in particular, low-*Kn* cases are characterized by substantially higher peak vapor velocities and relatively low interfacial condensation rates, when compared to high-*Kn* cases.

C. Effective approach for arbitrary meniscus shapes

All the results presented so far have considered a flat meniscus. Here we consider five different meniscus shapes (S_1–S_5 as illustrated in Fig. 1 in Sec. II) to study the impact of the interface curvature on the evaporation dynamics and the applicability of the effective evaporation coefficient approach for arbitrary meniscus shapes. It is to be noted here that the interface shape is predominantly determined by capillarity and therefore expected to have concave circular shapes as considered in this work. Additionally, convex circular shapes are not of interest here, as they will not have the desired effect of acting as a capillary pump. Therefore, *arbitrary* meniscus shapes, as mentioned in this work, strictly refer to typical concave circular shapes in the context of the nanoporous membrane application. The interface surface length (S), contact angle (θ), and radius of curvature (R) for an arbitrary meniscus are shown in Fig. 2. The interfaces S_1 to S_5 have a contact angle, θ of approximately 0°, 30°, 60°, 75°, and 90°, respectively. Here we focus only on the high Knudsen number regime, where the effective evaporation approach is expected to work better (as explained in Sec. III B for the flat interface). To illustrate the similarity between the

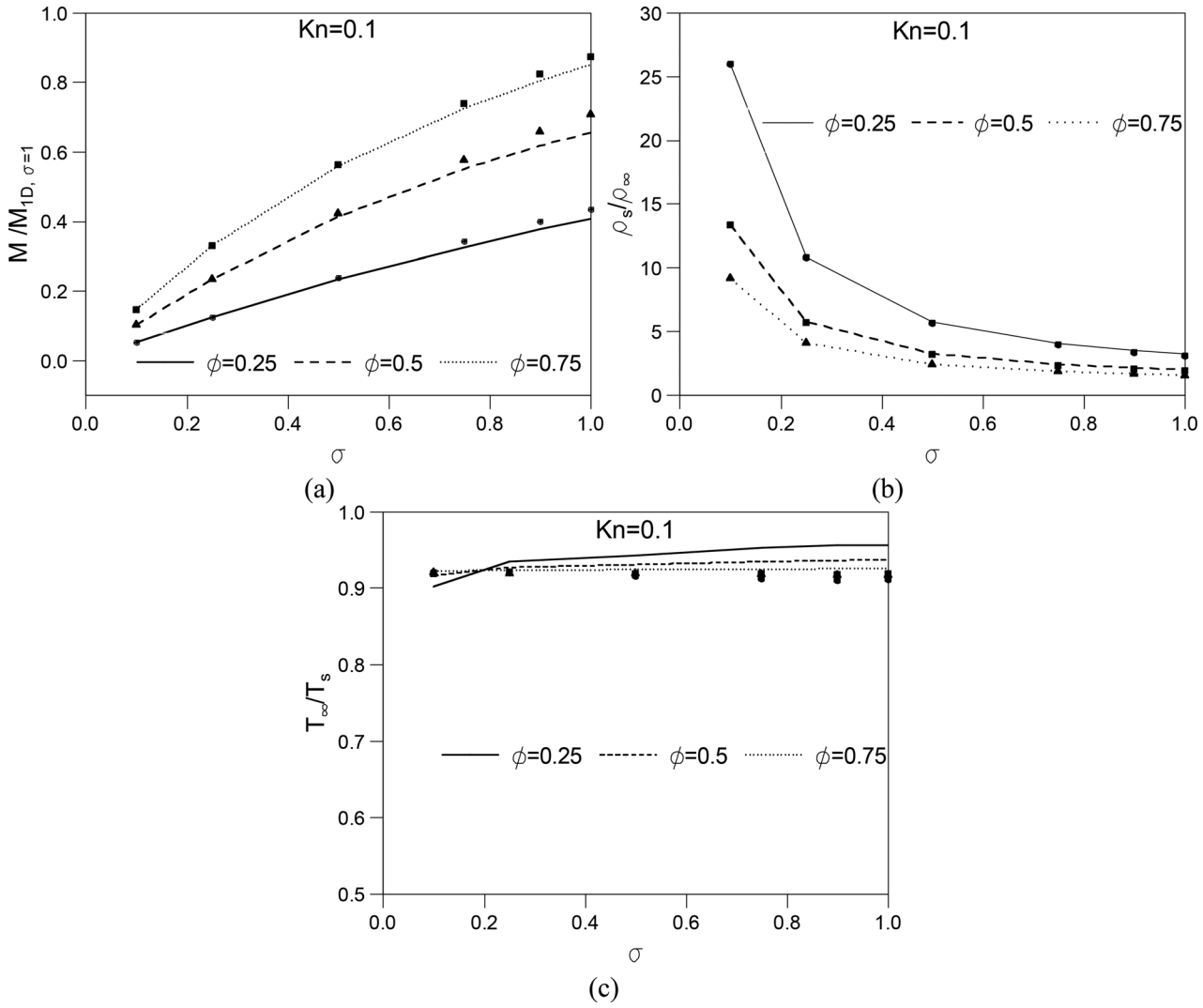

FIG. 8. (a) Normalized mass flux, (b) density jump, and (c) temperature jump vs the evaporation coefficient for $Kn = 0.1$ and $U_\infty = 60$ m/s when $\phi < 1$. The lines represent the analytical results; the symbols represent the DSMC results.

curved and flat interfaces, the velocity flow field and streamlines at two extreme Knudsen numbers, $Kn = 0.05$ and $Kn = 10$, are compared for a selected interface, S_5 and porosity, $\phi = 0.25$. The velocity field overlaid with streamlines for the two cases is compared in Fig. 12. Similar to the flat interface scenario, the flow-field is mostly two-dimensional for $\mathrm{Kn} = 0.05$, with the existence of a pair of Moffatt eddies. However, for larger Knudsen numbers ($Kn = 10$), the two-dimensionality of flow near the interface is comparatively minimal. This again implies that the overall one-dimensionality of flow underlying the effective evaporation coefficient approach works much better at high Knudsen numbers, even for the curved interfaces.

For an arbitrary meniscus, the choice of the effective evaporation coefficient parameter is not obvious as for a flat interface, since it is dependent on the meniscus curvature considered. For this more general case, the influence of different parameters like interface shape, porosity, and evaporation coefficient is encompassed by a single effective evaporation coefficient parameter. Here, σ_{eff} is thus determined indirectly from the analytical equations [Eqs. (4) and (6)] using the numerical mass fluxes provided by DSMC simulations. A constant Knudsen number, $Kn = 10$ and freestream velocity, $U_\infty = 60$ m/s has been considered for all the results reported in this section. The variation in the normalized evaporation rates and derived effective sigma values for various cases of porosity and evaporation coefficient is shown in Fig. 13 for two selected menisci (the semicircle meniscus, S_5 and the intermediate curved meniscus case, S_3). The evaporation rates as a function of the evaporation coefficient for the different porosities considered are shown in Fig. 13(a). It can be noted that the absolute magnitude of mass flux becomes lower as the evaporation coefficient reduces, as expected for all menisci. More interestingly, the variations in mass flux between the meniscus cases is noted to be minimal when

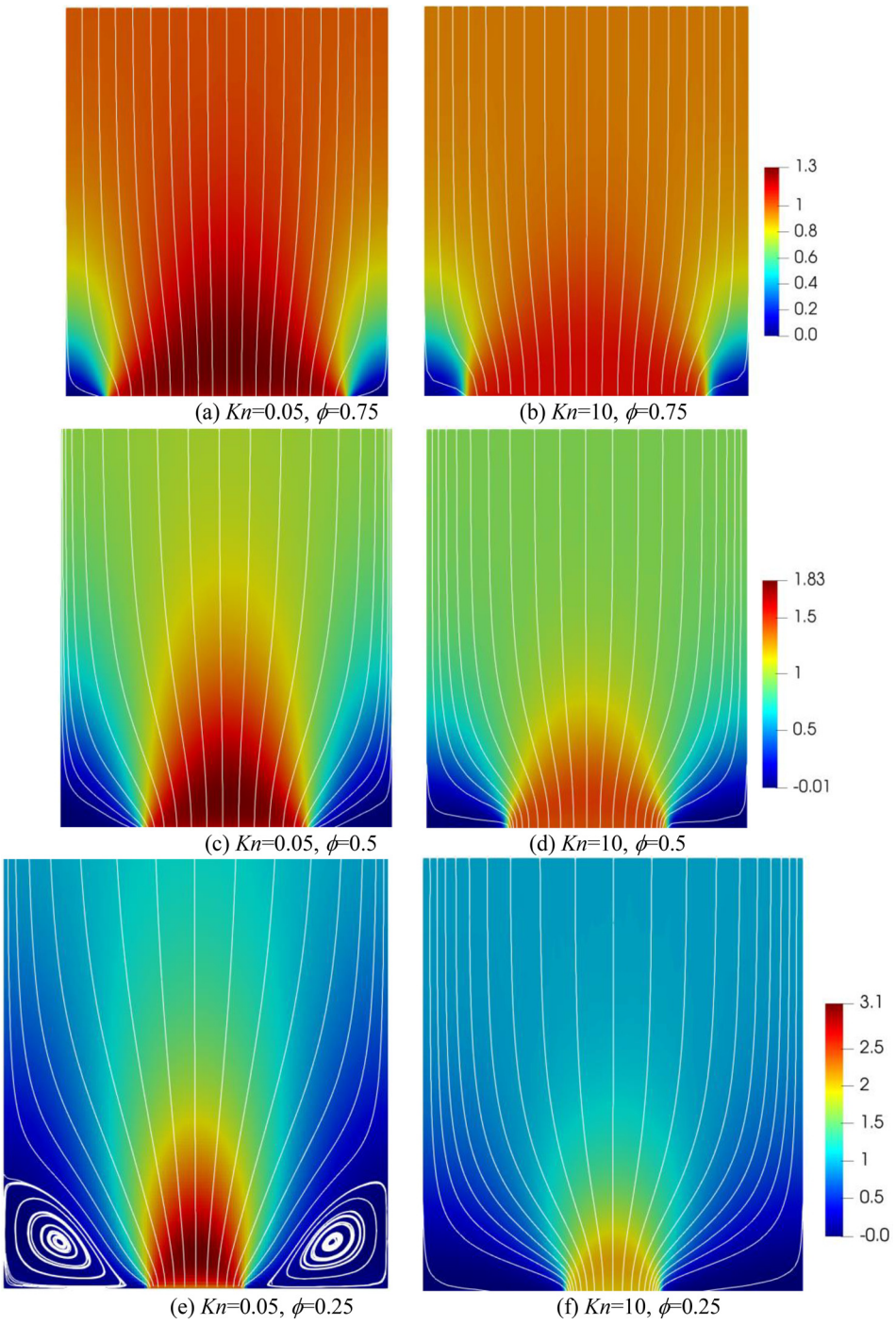

FIG. 9. Flow-fields near the interface showing the variation of normalized *y*-velocity, u/U_∞ overlaid with velocity streamlines for the flat meniscus cases, $\phi = 0.75$, 0.5, and 0.25 and two Knudsen numbers, $Kn = 0.05$ and $Kn = 10$. A constant far-field velocity, $U_\infty = 60$ m/s, is considered for all cases. (a) $Kn = 0.05$, $\phi = 0.75$; (b) $Kn = 10$, $\phi = 0.75$; (c) $Kn = 0.05$, $\phi = 0.5$; (d) $Kn = 10$, $\phi = 0.5$ (e) $Kn = 0.05$, $\phi = 0.25$; and (f) $Kn = 10$, $\phi = 0.25$.

$\sigma = 1$. In other words, as $\sigma \to 1$, the effective evaporation coefficient parameter for a curved interface simplifies to that for the flat mensicus case as $\sigma_{eff} \to (\phi \times \sigma)$, regardless of the contact angle or curvature of the meniscus shape considered. However, as σ reduces, the mass flux becomes proportional to the interface surface (i.e., area per unit width). This can be particularly noted for $\sigma \to 0$, as the semicircle meniscus, S_5 attains a significantly higher mass flux relative to the curved meniscus case, S_3.

The σ_{eff} for the two selected interfaces are shown in Fig. 13(b) for various cases of porosity and evaporation coefficient. It can be inferred from the plots that σ_{eff} scales with the porosity, e.g., $\sigma_{eff}|_{\phi=0.25} = 0.25 \times \sigma_{eff}|_{\phi=1}$. An empirical relation, which can very

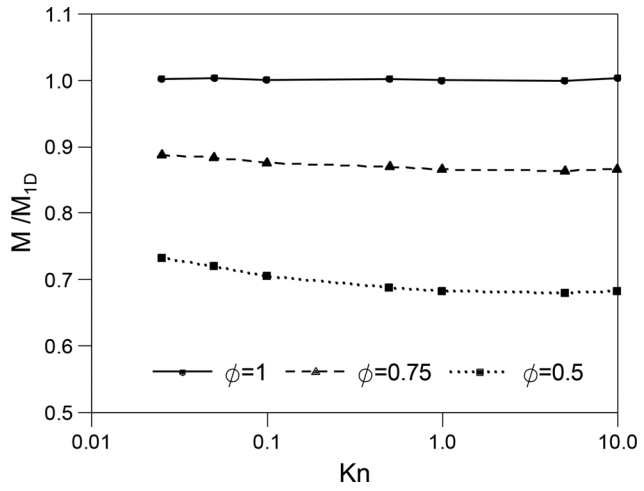

FIG. 10. Normalized mass flux vs the Knudsen number plotted for different porosities.

accurately predict the effective sigma for a wide range of typical meniscus configurations as a function of the interface surface (S), σ and ϕ have been fitted, and this is shown in Eq. (10). This relation is valid and general for a range of parametric space: ($0 \leq \theta \leq \pi/2$ rad), ($0.1 \leq \sigma \leq 1$), and ($0.25 \leq \phi \leq 1$),

$$\sigma_{eff} = \phi \times \begin{pmatrix} -0.202S'^3 - 0.031S'^2\sigma + 0.741S'^2 - 0.688S'\sigma^2 \\ +0.726S'\sigma - 0.855S' + 0.035\sigma^3 \\ +0.605\sigma^2 + 0.357\sigma + 0.311 \end{pmatrix}. \tag{10}$$

Here $S' = S/L_p$, where S is the interface surface length defined by $S = L_p \frac{\theta}{\sin(\theta)}$ so that Eq. (10) can be conveniently expressed in terms of either the interface surface or the contact angle.

TABLE II. Computed condensation rates, M_C, for different Knudsen numbers at $\phi = 0.5$ and $U_\infty = 60$ m/s.

Kn	M_C
0.05	0.325
0.1	0.337
1	0.358
10	0.361

σ_{eff} derived from the above empirical equation has been found to work very well in predicting the density and temperature jumps accurately for arbitrary interfaces. The agreement of the predicted density and temperature jump values from the effective one-dimensional approach with the corresponding DSMC results is illustrated in Fig. 14 for a selected interface, S_2. The agreement in results is clearly excellent. To confirm the validity of the effective one-dimensional approach at other conditions, we have carried out selected additional simulations at other relatively high Knudsen numbers (e.g., $Kn = 1$) and arbitrary far-field velocities ($30 < U_\infty < 240$ m/s) and compared the results against those predicted by the effective one-dimensional approach using Eq. (10). The results (not shown here for the sake of brevity and avoiding repetition) show excellent agreement with the DSMC results, similar to those observed for the case of a flat interface detailed in Sec. III A. This also confirms that for any case of fixed arbitrary meniscus shape, the value of the effective evaporation coefficient parameter is a constant for all far-field conditions (just as in the case of a flat interface) and can be predicted accurately from Eq. (10). To summarize the results for arbitrary interface shapes, it can be inferred that the effective one-dimensional approach works excellently, regardless of the far-field conditions and evaporation coefficients considered, as long as the interface Knudsen number considered is sufficiently large (i.e., $Kn > 0.1$).

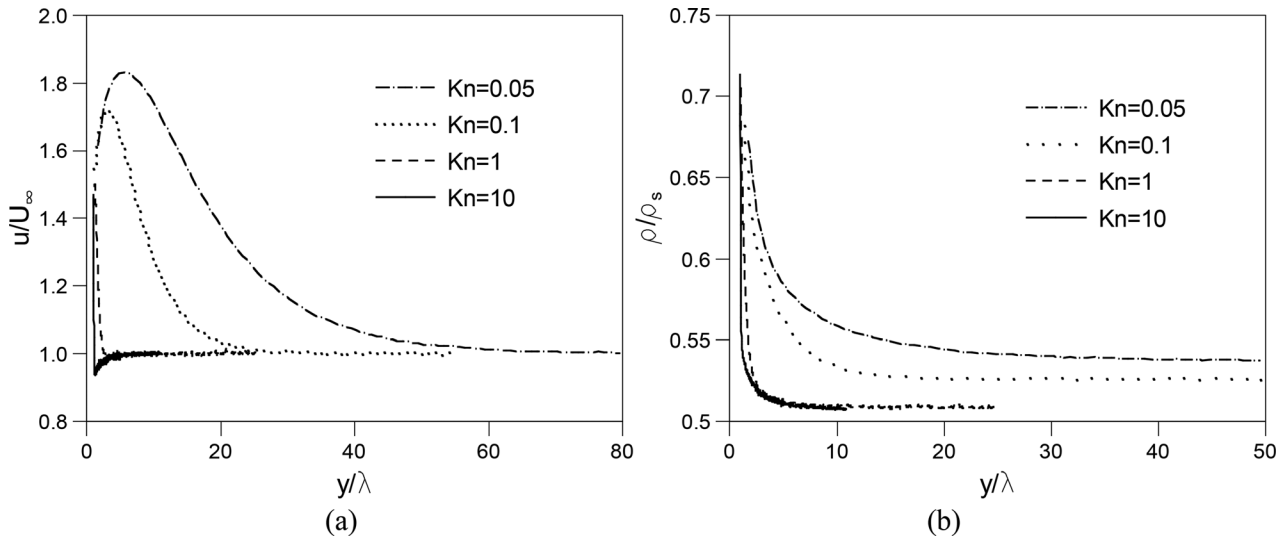

FIG. 11. Variation in (a) normalized flow velocity and (b) density profile along the extent of the computational domain. Only a small section next to the interface is shown.

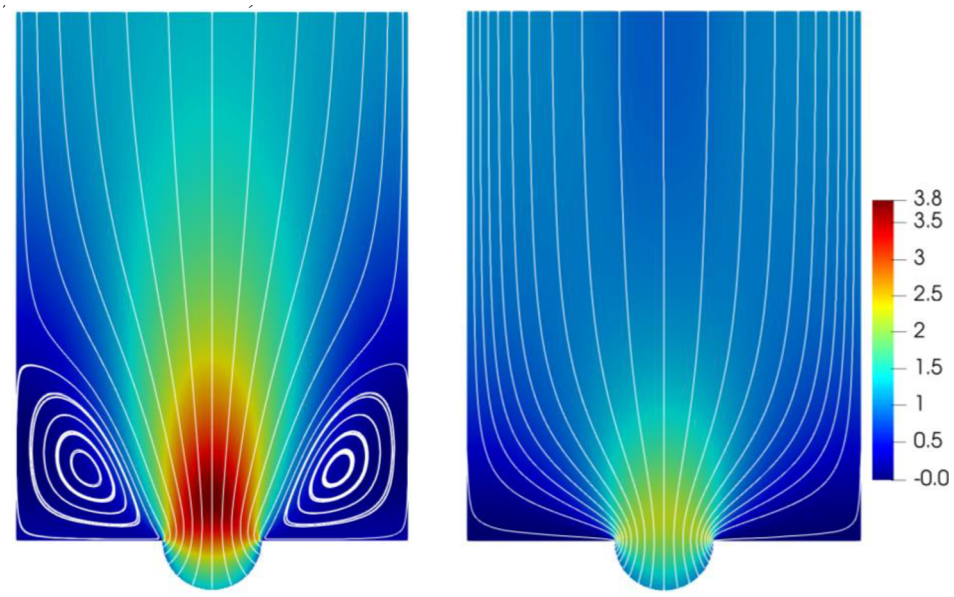

FIG. 12. Flow fields near the interface showing the variation of normalized *y*-velocity, u/U_∞ overlaid with velocity streamlines for the interface, S_5 at $\phi = 0.25$ and two Knudsen numbers: (a) $Kn = 0.05$ and (b) $Kn = 10$. A constant far-field velocity, $U_\infty = 60$ m/s, is considered.

D. Receding meniscus cases

So far, we have considered an ideal meniscus case, i.e., when the meniscus is pinned to the top of the pore. In practice, the meniscus could actually recede down the pore under adverse operating conditions. Figure 15 illustrates the receding interface shapes. Selected cases of receding heights, H are considered in the range $0 \leq H \leq 2L_p$. The interface shapes (S_1–S_5), are again considered to study the evaporation process, as done previously for the pinned meniscus cases. A constant Knudsen number, $Kn = 10$ and freestream velocity, $U_\infty = 60$ m/s have been considered for all the cases in this part of the study.

As for the pinned curved interface case described in Sec. III C, the effective evaporation coefficient σ_{eff} for any receding arbitrary curved meniscus has been derived indirectly from the corresponding computed DSMC mass fluxes and using Eqs. (4) and (6). An empirical relation which can very accurately predict the effective sigma for a wide range of typical meniscus configurations as a function of S, H, σ, and ϕ have been fitted, and this is shown in Eq. (11). This relation is

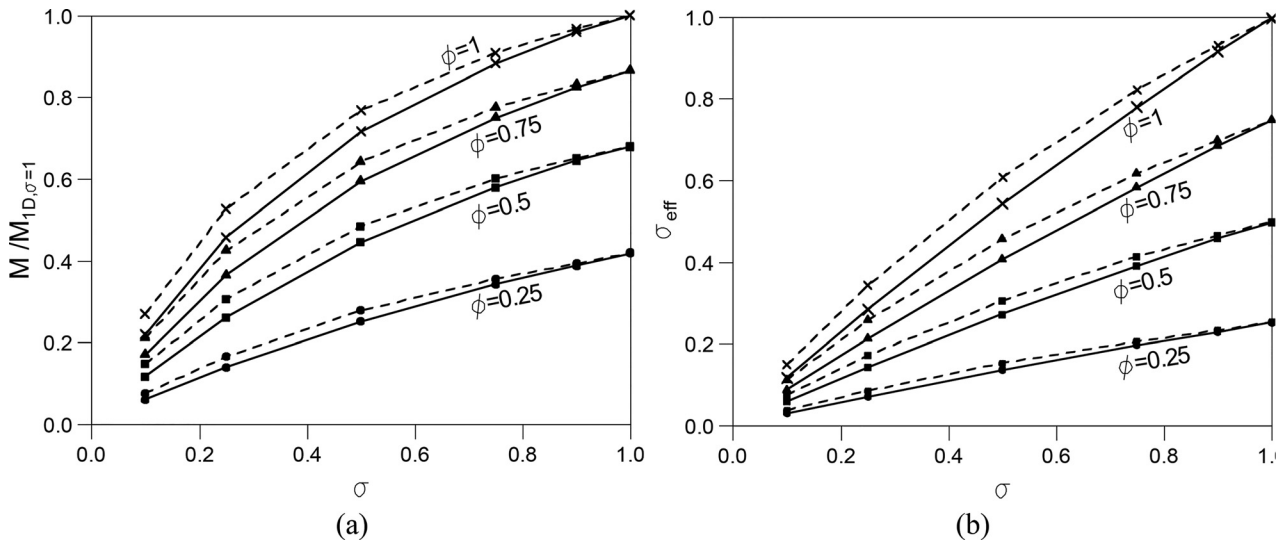

FIG. 13. (a) Mass flux and (b) the effective evaporation coefficient plotted as a function of the actual evaporation coefficient for various porosities at $Kn = 10$ and $U_\infty = 60$ m/s for the semicircle meniscus, S_5 and the intermediate curved meniscus, S_3. The solid lines refer to semicircle meniscus, S_5 and the dotted lines refer to the intermediate curved meniscus, S_3.

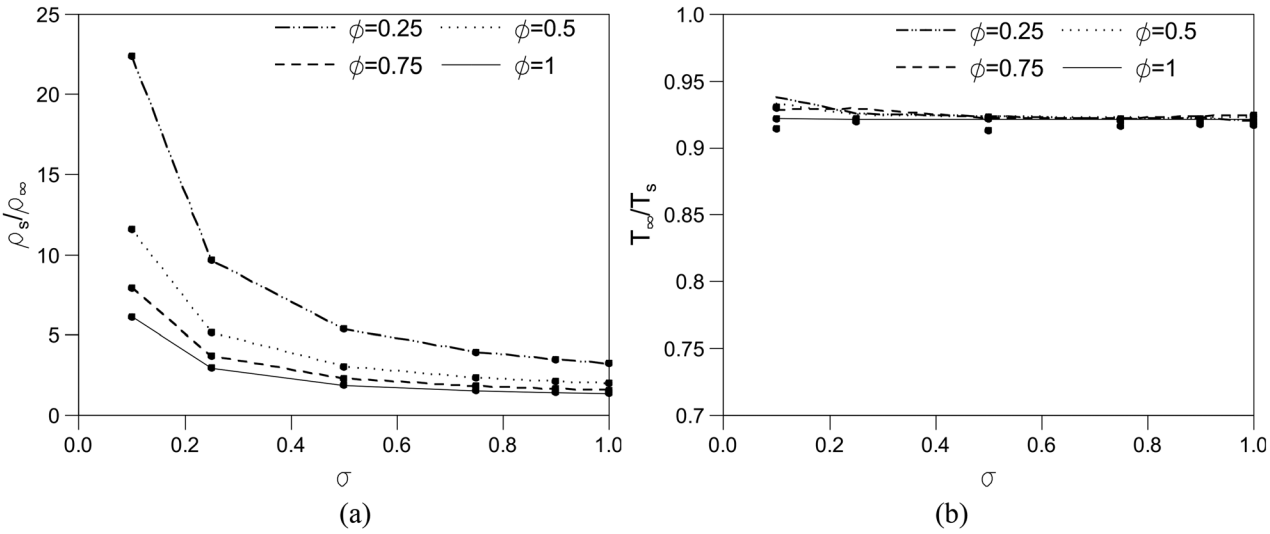

FIG. 14. (a) Density and (b) temperature jump values for various evaporation coefficients and porosities for interface, S_2. The results are for $Kn = 10$ and $U_\infty = 60$ m/s. Symbols denote DSMC results.

valid and general for a wide range of parameters: $(0 \le \theta \le \pi/2\,\text{rad})$, $(0.25 \le \sigma \le 1)$, $(0 \le H \le 2L_p)$, and $(0.25 \le \phi \le 1)$. It can be noted from Eq. (11) that σ_{eff} scales with porosity, i.e., if the effective evaporation coefficient for a particular nanoporous membrane configuration is known, the corresponding σ_{eff} at any other porosity can be obtained by simply multiplying it by ϕ,

$$\sigma_{eff} = \phi \times \begin{pmatrix} -0.012S'^3 + 0.057S'^2\sigma + 0.018S'^2h - 0.06S'^2 \\ -0.448S'\sigma^2 + 0.028S'\sigma h + 0.208S'\sigma \\ +0.009S'h^2 - 0.113S'h + 0.325S' + 0.071\sigma^3 \\ -0.046\sigma^2 h + 0.211\sigma^2 + 0.109\sigma h^2 \\ -0.454\sigma h + 0.933\sigma - 0.080h^3 + 0.158h^2 \\ +0.113h - 0.290 \end{pmatrix}. \tag{11}$$

Here $S' = S/L_p$, where S, the interface surface length is defined as $S = L_p \frac{\theta}{\sin(\theta)}$ and $h = \frac{H}{L_p}$.

Figure 16 shows the variation in the normalized evaporation rates and derived effective sigma values as a function of the receding height for arbitrary evaporation coefficients and a fixed porosity, i.e., $\phi = 0.5$. Results for two selected interfaces, i.e., the semicircle meniscus, S_5, and the flat meniscus, S_1, are shown. The trend in the variation of evaporation rate and effective sigma is very similar. From the evaporation rates plot, it can be noted that although the absolute value of mass flux decreases as σ reduces, the relative mass flux reduction (losses) as the meniscus recedes down the pore becomes minimal for very low values of σ. This can be attributed to the fact that as $\sigma \to 0$, a larger fraction of the molecules (proportional to $1-\sigma$), crossing the interface gets re-emitted thereby reducing the relative losses. Furthermore, it can be noted that as $\sigma \to 1$, the meniscus shape is not important as both the curved and flat menisci produce essentially the same evaporation rates for all receding heights considered. However, for very low values of σ, the evaporation rates are clearly very dependent on the meniscus shape and mass flux becomes proportional to the interface surface. In particular, as $\sigma \to 0$, the ratio of mass flux predicted by the semicircle meniscus to that by the flat meniscus approaches $\pi/2$ (the ratio of the semicircle meniscus to the flat meniscus).

The effective evaporation coefficient, one-dimensional analytical approach works excellently in predicting the density and temperature jumps accurately for any typical nanoporous membrane configuration. Agreement of the computed DSMC jump relations with the effective sigma approach results for the interface, S_5 is illustrated in Fig. 17. The agreement for both density and temperature jumps is excellent. The temperature jump has been found to be fairly insensitive to the change in parameters, i.e., for fixed free stream conditions the temperature attains a constant value regardless of the receding height, porosity, or evaporation coefficient. Selected simulations have been carried out at

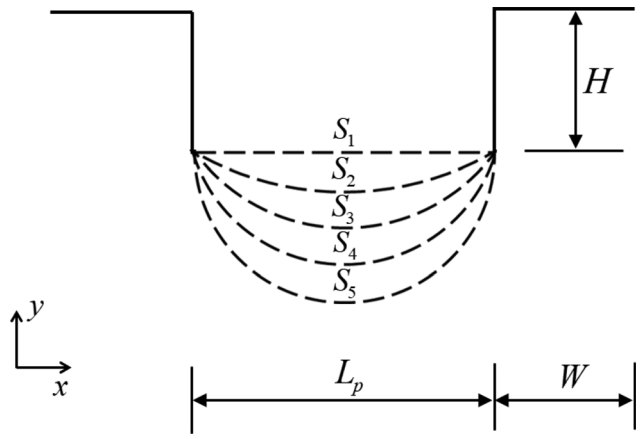

FIG. 15. Schematic of the different interfaces considered. Pinned cases ($h = 0$) are considered here.

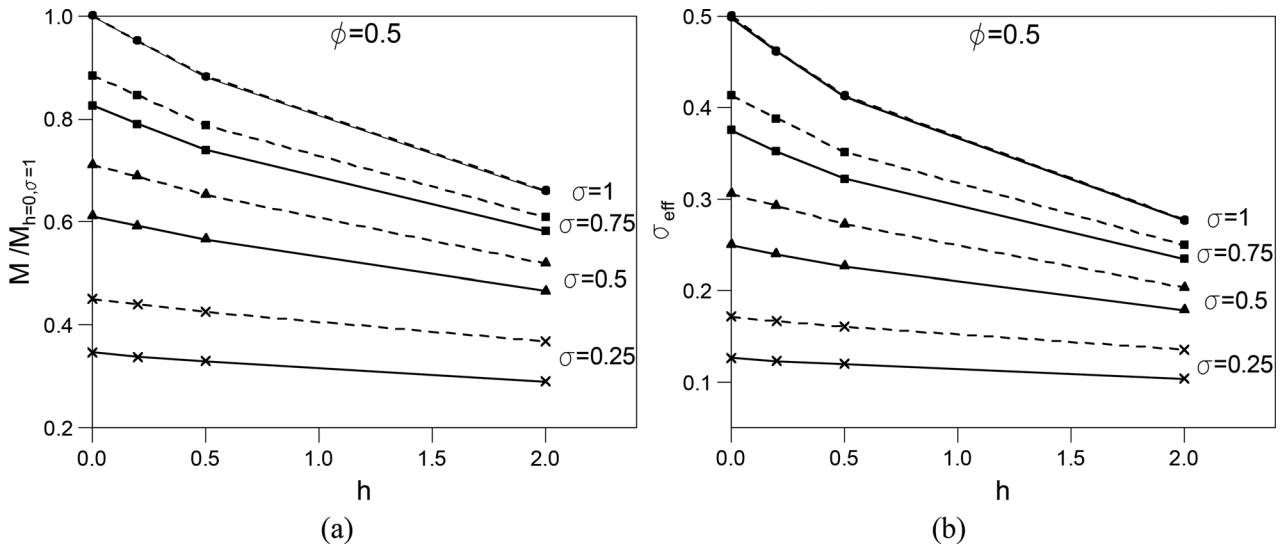

FIG. 16. The computed (a) normalized evaporation rates and (b) derived effective evaporation coefficients vs the receding height for $\phi = 0.5$, $Kn = 10$ and $U_\infty = 60$ m/s. Dotted lines represent the semicircle meniscus, S_5 and the solid lines represent the flat meniscus, S_1. The solid symbols denote DSMC results.

$Kn = 1$ and other far-field velocity conditions to confirm the accuracy of the effective one-dimensional approach at these other conditions. It has been found again that just as in the pinned cases for arbitrary curved menisci, the effective one-dimensional approach works equally well for the receding cases as well, so long as sufficiently large interface Knudsen numbers ($\sim Kn > 0.1$) are considered. Additionally, for a particular nanoporous membrane configuration, the value of the effective evaporation coefficient parameter is a constant for all far-field conditions and can be predicted accurately from Eq. (11).

IV. CONCLUSIONS

In the present study, an effective one-dimensional analytical approach has been proposed to predict the evaporation output parameters for two-dimensional arbitrary nanoporous configurations. Specifically, the two-dimensional nanoporous membrane evaporation problem has been simplified into an effective one-dimensional problem, by the introduction of an effective evaporation coefficient parameter. Our proposed approach provides, inexpensively, accurate results for all typical evaporation output parameters like evaporative mass flux and jump relations across the Knudsen layer, for a wide range of system

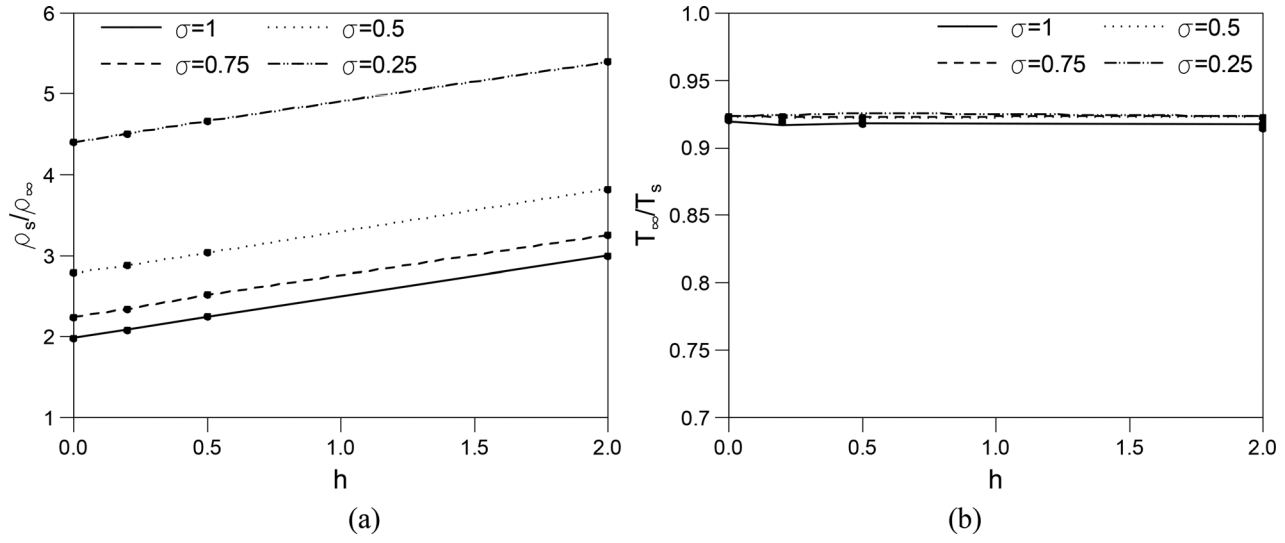

FIG. 17. (a) Density and (b) temperature jump values for various evaporation coefficients and receding heights. The results are for interface, S_5 computed at $\phi = 0.5$, $Kn = 10$ and $U_\infty = 60$ m/s. Lines denote results from the effective sigma approach and symbols denote DSMC results.

parameters. For a flat interface, the effective evaporation coefficient can be obtained by directly relating the porosity of the membrane to the actual evaporation coefficient. For an arbitrary nanoporous membrane configuration, it has been shown that the influence of different parameters like meniscus shape, evaporation coefficient, porosity, and receding heights can still be lumped into a single effective evaporation coefficient parameter. A wide range of parameter space covering relevant combinations of porosity, evaporation coefficient, meniscus shape, and receding menisci at various operating conditions have been considered to demonstrate the feasibility of the effective evaporation coefficient approach. The accuracy of this effective approach has been demonstrated with the aid of extensive DSMC simulations. It is shown that for the nanoporous membrane evaporation problem, where the Knudsen numbers are sufficiently large (i.e., in the upper transition or free molecular regime), the effective approach works accurately for arbitrary membrane configurations regardless of the far-field conditions and evaporation coefficients considered. At smaller Knudsen numbers ($Kn \leq 0.1$), however, discrepancies have been found, which can be attributed to the variation in the interfacial processes at different Knudsen numbers.

In summary, our work has enabled an efficient and accurate means of predicting many typical evaporation output parameters for a wide range of possible membrane configurations, thereby aiding the engineering analysis and design of nanoporous membrane-based cooling devices. Finally, future work will consider three-dimensional simulations to investigate the effects of multi-dimensionality on the evaporation dynamics for nanoporous membranes.

ACKNOWLEDGMENTS

This work was supported through the United Kingdom Engineering and Physical Sciences Research Council under Grant No. EP/N016602/1—"Nano-Engineered Flow Technologies: Simulation for Design across Scale and Phase." BJ and DRE acknowledges additional support from United Kingdom Science and Technology Facilities Council (STFC) under Grant No. ST/R006733/1. The simulations in this work were carried out on the UK's National Supercomputing service, ARCHER.

DATA AVAILABILITY

The data that support the findings of this study are available from the corresponding author upon reasonable request.

REFERENCES

[1]S. S. Sazhin, "Modelling of fuel droplet heating and evaporation: Recent results and unsolved problems," Fuel **196**, 69 (2017).
[2]M. Chang, Z. Lee, S. Park, and S. Park, "Characteristics of flash boiling and its effects on spray behavior in gasoline direct injection injectors: A review," Fuel **271**, 117600 (2020).
[3]Y. Li and S.-L. Xu, "DSMC simulation of vapor flow in molecular distillation," Vacuum **110**, 40 (2014).
[4]G. Pinto, F. Silva, J. Porteiro, J. Míguez, and A. Baptista, "Numerical simulation applied to PVD reactors: An overview," Coatings **8**, 410 (2018).
[5]J. Lee, T. Laoui, and R. Karnik, "Nanofluidic transport governed by the liquid/vapor interface," Nat. Nanotechnol. **9**, 317 (2014).
[6]D. L. Gin and R. D. Noble, "Designing the next generation of chemical separation membranes," Science **332**(6030), 674 (2011).
[7]X. Liu, M. H. Hu, C. G. Caneau, R. Bhat, and C.-E. Zah, "Thermal management strategies for high power semiconductor pump lasers," IEEE Trans. Compon. Packag. Manuf. Technol. **29**(2), 268 (2006).
[8]E. Pop, "Energy dissipation and transport in nanoscale devices," Nano Res. **3**(3), 147 (2010).
[9]R. S. Pengelly, S. M. Wood, J. W. Milligan, S. T. Sheppard, and W. L. Pribble, "A review of GaN on SiC high electron mobility power transistors and MMICs," IEEE Trans. Microwave Theory Tech. **60**(6), 1764 (2012).
[10]S. You, J. Kim, and K. Kim, "Effect of nanoparticles on critical heat flux of water in pool boiling heat transfer," Appl. Phys. Lett. **83**(16), 3374 (2003).
[11]R. Chen, M.-C. Lu, V. Srinivasan, Z. Wang, H. H. Cho, and A. Majumdar, "Nanowires for enhanced boiling heat transfer," Nano Lett. **9**(2), 548 (2009).
[12]S. G. Kandlikar, "Fundamental issues related to flow boiling in minichannels and microchannels," Exp. Therm. Fluid Sci. **26**(2), 389 (2002).
[13]L. Lin and R. Ponnappan, "Heat transfer characteristics of spray cooling in a closed loop," Int. J. Heat Mass Transfer **46**(20), 3737 (2003).
[14]Z. Lu, T. R. Salamon, S. Narayanan, K. R. Bagnall, D. F. Hanks, D. S. Antao, B. Barabadi, J. Sircar, M. E. Simon, and E. N. Wang, "Design and modeling of membrane-based evaporative cooling devices for thermal management of high heat fluxes," IEEE Trans. Compon. Packag. Manuf. Technol. **6**, 1056 (2016).
[15]L. Swanson and G. Herdt, "Model of the evaporating meniscus in a capillary tube," J. Heat Transfer **114**, 434 (1992).
[16]H. Wang, S. V. Garimella, and J. Y. Murthy, "Characteristics of an evaporating thin film in a microchannel," Int. J. Heat Mass Transfer **50**, 3933 (2007).
[17]S. Narayanan, A. G. Fedorov, and Y. K. Joshi, "Interfacial transport of evaporating water confined in nanopores," Langmuir **27**, 10666 (2011).
[18]Z. Lu, S. Narayanan, and E. N. Wang, "Modeling of evaporation from nanopores with nonequilibrium and nonlocal effects," Langmuir **31**(36), 9817 (2015).
[19]T. Humplik, J. Lee, S. O'Hern, B. Fellman, M. Baig, S. Hassan, M. Atieh, F. Rahman, T. Laoui, and R. Karnik, "Nanostructured materials for water desalination," Nanotechnology **22**, 292001 (2011).
[20]T. Ytrehus, "Molecular-flow effects in evaporation and condensation at interfaces," Multiphase Sci. Technol. **9**, 205 (1997).
[21]B. John, R. Enright, J. E. Sprittles, L. Gibelli, D. R. Emerson, and D. A. Lockerby, "Numerical investigation of nanoporous evaporation using direct simulation Monte Carlo," Phys. Rev. Fluids **4**, 113401 (2019).
[22]K. L. Wilke, B. Barabadi, Z. Lu, T. Zhang, and E. N. Wang, "Parametric study of thin film evaporation from nanoporous membranes," Appl. Phys. Lett. **111**, 171603 (2017).
[23]J. Lee and R. Karnik, "Desalination of water by vapor-phase transport through hydrophobic nanopores," J. Appl. Phys. **108**, 044315 (2010).
[24]Z. Lu, I. Kinefuchi, K. Wilke, G. Vaartstra, and E. Wang, "A unified relationship for evaporation kinetics at low Mach numbers," Nat. Commun. **10**, 2368 (2019).
[25]Q. Wang, Y. Shi, and R. Chen, "Transition between thin film boiling and evaporation on nanoporous membranes near the kinetic limit," Int. J. Heat Mass Transfer **154**, 119673 (2020).
[26]D. F. Hanks, Z. Lu, J. Sircar, I. Kinefuchi, K. R. Bagnall, T. R. Salamon, D. S. Antao, B. Barabadi, and E. N. Wang, "High heat flux evaporation of low surface tension liquids from nanoporous membranes," ACS Appl. Mater. Interfaces **12**, 7232 (2020).
[27]G. Xia, J. Wang, W. Zhou, D. Ma, and J. Wang, "Orientation effects on liquid-vapor phase change heat transfer on nanoporous membranes," Int. Commun. Heat Mass Transfer **119**, 104934 (2020).
[28]H. Hertz, "Ü ber die Verdunstung der Flüssigkeiten, insbesondere des Quecksilbers, im luftleeren Raume," Ann. Phys. **253**, 177 (1882).
[29]M. Knudsen, "Die maximale Verdampfungsgeschwindigkeit des Quecksilbers," Ann. Phys. **352**, 697 (1915).
[30]R. W. Schrage, *A Theoretical Study of Interphase Mass Transfer* (Columbia University Press, New York, 1953).
[31]J. W. Rose, "Accurate approximate equations for intensive subsonic evaporation," Int. J. Heat Mass Transfer **43**, 3869 (2000).
[32]D. Labuntsov and A. Kryukov, "Analysis of intensive evaporation and condensation," Int. J. Heat Mass Transfer **22**, 989 (1979).
[33]Y. Sone, "Kinetic theoretical studies of the half-space problem of evaporation and condensation," Transp. Theory Stat. Phys. **29**, 227 (2000).
[34]A. A. Avdeev and Y. B. Zudin, "Kinetic analysis of intensive evaporation (method of reverse balances)," High Temp. **50**, 527 (2012).
[35]A. Frezzotti, "Boundary conditions at the vapor-liquid interface," Phys. Fluids **23**, 030609 (2011).

[36]A. Frezzotti, "A numerical investigation of the steady evaporation of a polyatomic gas," Eur. J. Mech. B/Fluids **26**, 93 (2007).
[37]S. J. Plimpton and M. A. Gallis, "SPARTA Direct Simulation Monte Carlo (DSMC) Simulator" (2015), see http://sparta.sandia.gov
[38]S. J. Plimpton, S. G. Moore, A. Borner, A. K. Stagg, T. P. Koehler, J. R. Torczynski, and M. A. Gallis, "Direct simulation Monte Carlo on petaflop supercomputers and beyond," Phys. Fluids **31**, 086101 (2019).
[39]G. A. Bird, *Molecular Gas Dynamics and the Direct Simulation of Gas Flows* (Clarendon, Oxford, 1998).
[40]M. Maerefat, S. Fujikawa, T. Akamatsu, and T. Mizutani, "An experimental study of non-equilibrium vapor condensation in a shock-tube," Exp. Fluids **7**(8), 513 (1989).
[41]T. Tsuruta, T. Masuoka, and Y. Kato, "Estimation of condensation coefficient from dropwise condensation heat transfer," Therm. Sci. Eng. **2**(1), 98 (1994).
[42]S. Fujikawa and M. Maerefat, "A study of the molecular mechanism of vapor condensation," JSME Int. J. **33**(4), 634 (1990).
[43]M. Matsumoto, "Molecular dynamics of evaporation and condensation," in Proceedings of the 2nd International Conference on Multiphase Flow, Supplement, 1995, p. 69.
[44]M. Matsumoto, K. Yasuoka, and Y. Kataoka, "Evaporation and condensation at a liquid surface. II. Methanol," J. Chem. Phys. **101**(9), 7912 (1994).
[45]T. Tsuruta and G. Nagayama, "A microscopic formulation of condensation coefficient and interface transport phenomena," Energy **30**, 795 (2005).
[46]H. K. Moffatt, "Viscous and resistive eddies near a sharp corner," J. Fluid Mech. **18**, 1 (1964).